Impact of polymer structure in polyurethane topcoats on anti-icing properties

Donghyeon Lee[1], Junho Park[1], Min Ji Woo[2], Juhyeong Lee[3], Joung-Man Park[1], Hyung Mi Lim[4], Tae Kyung Lee[1], Seong Baek Yang[5,†], Sang Yong Nam[1,2,3,†], and Dong-Jun Kwon[1,2,5,†]

[1]Department of Materials Engineering and Convergence Technology, Gyeongsang National University, Jinju 52828, Republic of Korea

[2]School of Polymer Science and Engineering, Gyeongsang National University, Jinju 52828, Republic of Korea

[3]Department of Mechanical and Aerospace Engineering, Utah State University, Logan, UT 84322

[4]Aerospace Convergence Materials Center, Korea Institute of Ceramic Engineering and Technology, Jinju 52851, Republic of Korea

[5]Research Institute for Green Energy Convergence Technology, Gyeongsang National University, Jinju 52828, Republic of Korea

[†]To whom correspondence should be addressed.
E-mail: rorrir@empas.com, djkwon@gnu.ac.kr (Dong-Jun Kwon)
E-mail: waldem@gnu.ac.kr (Sang-Yong Nam)
E-mail: sbyang@gnu.ac.kr (Seong Baek Yang)

Abstracts

Icing on the topcoat layer of structures or mobility systems can be a factor leading to functional failures or accidents. Material engineering approach to prevent icing involves creating hydrophobic surfaces. In this study, it was confirmed that the method of controlling the structure of polymers using solvents to adjust surface hydrophobicity and ice prevention effects is effective. Polyurethane (PU) topcoats are primarily used on the exterior of mobility devices; therefore, structure of PU was manipulated using xylene. Through the adjustment of the ratio between PU and xylene, changes in the curing enthalpy and crystal structure were observed, which led to alterations in tensile strength. Additionally, changes in surface energy and contact angle occurred depends on xylene content, and de-icing property of PU topcoat was enhanced by 66 % on the surface of the 20 vol% xylene PU topcoat, compared to the pure PU topcoat. It was confirmed that the basic method of manipulating the polymer structure through solvent amount in topcoats could be utilized as a technique in hydrophobic surface research, such as ice prevention.

1. Introduction

Icing occurs when water solidifies into ice on the surface of a solid substrate. If icing occurs on structures or mobility devices, it can lead to malfunctions, operational shutdowns, or accidents. In the case of aircraft, icing can lead to increased drag and weight, potentially causing crash accidents [1, 2]. Icing on wind turbine blades can lead to a decrease in performance and cessation of operation [3]. In electric vehicles, there have been reported cases of operational interruptions in protruding doors and issues with opening and closing the charging port due to icing. To address such issues, research on surface modification and de-icing is being conducted by numerous researchers [4, 5].

Research applying de-icing systems through heating to mobility devices, studying optimal solvents introduced with chemical substances for ice removal, and examining hydrophobic surfaces based on physical roughness and chemical surface treatments can be considered as representative studies for delaying and preventing icing [6]. De-icing methods using heat include removing ice through the operational heat generated by devices such as aircraft jet engines, and electric heating de-icing methods [7]. In cases where heat is generated by device operation, if the heat is insufficient, it cannot be used for de-icing. Moreover, with the recent introduction of electric battery-powered mobility, the absence of engine-generated heat has eliminated a means of ice removal. Electric heating de-icing methods require additional energy to remove ice and are difficult to apply to dynamic parts, such as propellers. Research aimed at increasing the efficiency of de-icing includes studies on using solar heat and light for ice removal. Additionally, methods for removing ice through solar radiation and photothermal means are being investigated [8-10]. However, methods utilizing solar heat and light are limited to when the sun is up and cannot be used in shaded areas, presenting a significant limitation. Chemical de-icing methods involve the use of deicing solutions to remove ice. However, using

deicing solutions can lead to issues with the solution penetrating into device internals, and there are limitations to their real-time application on large structures or while mobility devices are in operation. Such limitations in application scope or circumstances highlight the need for research related to anti-icing techniques to delay and prevent icing.

Materials engineering approach to anti-icing involves controlling surface wettability. One approach involves creating hydrophilic surfaces to inhibit ice formation [11, 12]. These methods require either considerably high humidity or the formation of a surface lubrication layer. Another approach involves creating a hydrophobic surface [13]. Methods to achieve hydrophobic surfaces include creating surface roughness [14], or coating the surface with hydrophobic materials [15, 16]. Methods to create surface roughness include surface etching or the application of scratches [17]. Methods to achieve hydrophobic surfaces include creating patterns that mimic the shape of lotus leaves or forming honeycomb structures on the base surface. However, methods that involve creating surface roughness may lead to reduced hydrophobic performance due to wear or deformation of the base, and the etching process can be inefficient in terms of treatment time and cost. For hydrophobic coatings, there are methods involving the application of polymer coatings and coatings with added nanoparticles [18, 19]. Polymer coatings utilize hydrophobic polymers such as poly(vinylidene fluoride), siloxane, and polyurethane (PU) [20-22]. There are two types of approaches using nanoparticles: one involves applying hydrophobic nanoparticles to create hydrophobic surfaces [23, 24], and the other involves adding nanoparticles to increase surface roughness, thereby achieving hydrophobicity [25]. However, hydrophobic coating methods have limitations in terms of durability because nanoparticles can detach, or the nanoparticle-incorporated coating layer can wear away [26, 27].

In the construction of mobility infrastructures, the exterior surface is frequently encapsulated with a topcoat formulated from PU or epoxy compounds. This external layer serves a pivotal

role in safeguarding against environmental degradation, moisture infiltration, chemical exposure, and physical wear. The propensity for ice accretion on this topcoat necessitates the integration of hydrophobic features or the durable preservation of the substrate's hydrophobic characteristics as a significant aspect of its design consideration. Research trends concerning topcoats have predominantly focused on enhancing mechanical properties, aging resistance, and wear resistance [28, 29]. Optimization studies of topcoats, without resorting to additional processing techniques, are essential for improving their performance.

Through the structural control of polymer materials, it is possible to regulate mechanical properties and surface characteristics via alterations in polymer crystallinity, conformation of molecular chains, and molecular arrangement. Therefore, this study conducted research to enhance anti-icing performance by altering the polymer structure. To modify the polymer structure, the coating material was diluted in various concentrations of xylene for use. During the polymer coating process, as monomers or oligomers cure to form polymers, the diluent acts as a solvent and affects the reaction rate, leading to changes in the polymer structure. In the polymer coating process, as monomers or oligomers undergo curing to form polymers, the diluent serves as a solvent, influencing the reaction rate and thus altering the polymer structure. Fourier-transform infrared spectroscopy (FT-IR), differential scanning calorimetry (DSC), and X-ray diffraction (XRD) were employed to investigate the crystalline structure of polymers, confirming that the concentration variations of the solvent induce structural modifications in the polymers. Fractional free volume (FFV) within the material was examined through molecular dynamics (MD) simulation. Mechanical properties were assessed through tensile testing. Contact angle measurement, surface energy prediction, and work of adhesion calculation were conducted for surface characterization. Icing tests were conducted at −20 °C for anti-icing experiments in static and dynamic conditions.

2. Experimental sections

2.1. Materials

PU topcoat (Spirolltan, Samhwa, Korea) and xylene (Samchun chemicals, Korea) was used for the production of specimen. Twill weave prepreg (prepreg, Hankook Carbon, Korea) was utilized for the fabrication of carbon fiber reinforced plastic (CFRP), employing carbon fibers (T-700, Toray, Japan). Deionized water (Sigma Aldrich, USA), formamide (TCI, Japan), ethylene glycol (Daejung, Korea), and diiodomethane (Sigma Aldrich, USA) were employed for contact angle measurement.

2.2. Preparation of specimens and measurement of surface morphology

In this study, a two-component PU topcoat was used to coat CFRP. CFRP was fabricated using twill weave prepreg with T-700 fibers to a thickness of 2 mm. The diluent used in the coating was primarily from the xylene series. Two-component PU topcoat was used by mixing the base and the hardener at a volume ratio of 5:1, and experiments were carried out with xylene at volume ratios of 0, 10, 20, and 30 % concentrations, respectively. Viscosity of the mixed coating solution was measured using a Brookfield viscometer (Brookfield, DV-II, Australia). Samples were prepared by spray coating as illustrated in Fig.1. The spray gun (Anest Iwata, RG-3L, Japan) had a nozzle diameter of 0.4 mm, and the pressure during coating was set to 1 MPa. Coating condition and surface morphology of the specimens were analyzed using a confocal microscope (VK-X3000, Keyence, Japan), and the surface roughness of the specimens was measured according to ISO-4287 standards using a surface roughness tester (SJ-210, Mitutoyo, Japan).
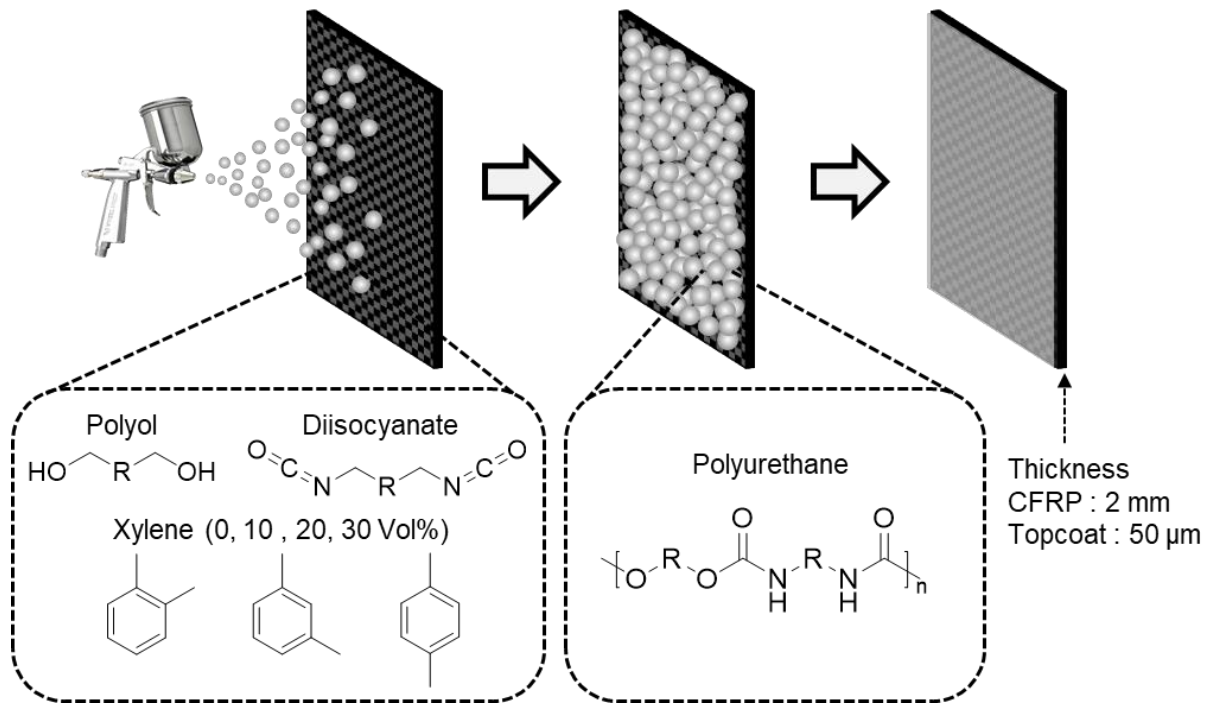
Figure 1. Schematic diagram of PU topcoat spray coating, behavior of coating droplets, and chemical structure of PU topcoat.

2.3. Verification of the molecular structure and reactivity about PU

Curing reaction rate and enthalpy change during curing of PU were examined using DSC (DSC Q20, TA Instruments, USA). The test analysis conditions involved diluting 5 mg of PU in xylene at various concentrations and placing it in an aluminum DSC dish. The results were obtained by maintaining the temperature at 25 °C. FT-IR (Nicolet iS5, Thermo Scientific, USA) was employed to investigate the structural changes in the PU topcoat's curing reaction. XRD (Miniflex, Rigaku, Japan) was used to analyze the crystallinity of PU at various concentrations, and the Scherrer equation was applied to determine the size of the crystals [30].

$$\tau = \frac{K\lambda}{\beta cos\theta} \tag{1}$$

Here, τ represents the average size of the crystallite (grain domain), K is shape factor, λ is X-ray wavelength, β is full width at half maximum (FWHM), and θ is X-ray incident angle (°).

2.4. Computational details

To investigate the free volume of PU topcoat, the MD simulations were performed by using COMPASS II forcefield [31]. The isothermal-isobaric ensemble (*i.e.*, *NPT* ensemble) was performed for 10 ns with 1 fs time step using Berendsen of thermostat and barostat [32] at 1 atm and 298 K. The atom-based summation and the particle-particle particle-mesh methods were used for van der Waals interaction with a cut-off distance of 12.5 Å and for the electrostatic interactions with 0.001 kcal/mol accuracy, respectively. The model systems for MD simulations were described in Fig. S1 and Table S1. Based on the previous The FFV was calculated using the following equation,

$$FFV = \frac{V_{total} - 1.3 \cdot V_{vdW}}{V_{total}} \tag{2}$$

where V_{total} and V_{vdw} are the total and the van der Waals volumes of system, respectively. The Bondi packing factor (*i.e.*, 1.3) was used to calculate the FFV in this study.

2.5. Evaluation of mechanical test of PU topcoat

Tensile testing was conducted to analyze the mechanical strength in relation to changes in PU structure and crystallinity. Tensile test was performed using a universal testing machine (LR-10K, LLOYD, USA) according to ASTM D882 standards (area = 10 mm × 1 mm, gauge length = 100 mm). Specimens for tensile test were prepared using a casting knife, and specimens were produced by casting on Teflon dish.

2.6. Contact angle measurement and evaluation of surface analysis depends on molecular structure of PU

Contact angle, surface energy, and work of adhesion were derived to investigate the surface characteristics of PU topcoat depends on xylene content [33]. Contact angles for DI water, formamide, ethylene glycol, and diiodomethane were measured using a static contact angle meter (L2004A1, Ossila, UK) through the goniometer method. Calculations were performed using the following Young's equation [34]:

$$\gamma_{SL} = \gamma_S + \gamma_L \cos \theta \tag{3}$$

Here, γ_{SL} is the solid/liquid interfacial free energy, γ_S is the solid surface energy, γ_L is the liquid surface energy, and θ is the contact angle.

The Fowkes model interprets surface energy by dividing it into the dispersion component (γ_S^d), related to London dispersion forces, and the polar component (γ_S^d), associated with the Keesom polar contribution [35]:

$$\gamma_S = \gamma_S^d + \gamma_S^p \tag{4}$$

Through their work, Owens, Wendt, Rabel, and Kaelble derived the following equation:

$$\gamma_{SL} = \gamma_S + \gamma_L - 2(\gamma_{Sa}\gamma_{Ld})^{1/2} - 2(\gamma_{Sp}\gamma_{Lp})^{1/2} \tag{5}$$

Work of adhesion with water and ice was calculated using the obtained surface energy. The surface tension of the standard solution was used for water, and the surface energy of ice was determined at the experimental temperature of −20 °C by measuring the contact angle, using the same method employed to calculate the specimen's surface energy. According to the Owens-method, work of adhesion can be calculated using the following formula [36]:

$$W_a = 2(\sqrt{\gamma_{d1}\gamma_{d2}} + \sqrt{\gamma_{p1}\gamma_{p2}}) \tag{6}$$

2.7. Evaluation of anti-icing properties depends on molecular structure of PU

Icing tests were conducted to evaluate the anti-icing performance of CFRP and polyurethane topcoat. Experimental conditions were set at 40 % humidity and −20 °C. The ambient air and water vapor were also stabilized at the set temperature over a period of 4 h. Subsequently, the specimen was placed on top of the chamber and the experiment was conducted for 10 min. USB microscope (AM3113, AnMo Electronics Corporation, Taiwan) was utilized to document the pattern and timing of ice formation. Onset of icing was measured by observing the formation of white ice and the coverage of ice in the recorded video. Ice was subsequently removed using a deicing solution, a 1:1 mixture of ethylene glycol and distilled water. This procedure was repeated five times to assess changes in the delay time of ice formation due to the deicing.

Wind tunnel test was conducted to investigate the anti-icing performance of CFRP and a polyurethane topcoat under dynamic conditions. Experimental conditions were established to match those of the previous icing test, with a humidity level of 40 % and a temperature of −20 °C. The surrounding air and water vapor were stabilized at the set temperature over a period of 4 h. During the experiment, wind was blown at a speed of 10 m/s using a blower, and the specimen was placed on top of the chamber for a duration of 10 min. Setup for the experiment was prepared as shown in Fig. 2 [37, 38]. USB microscope was used to observe the formation of ice.
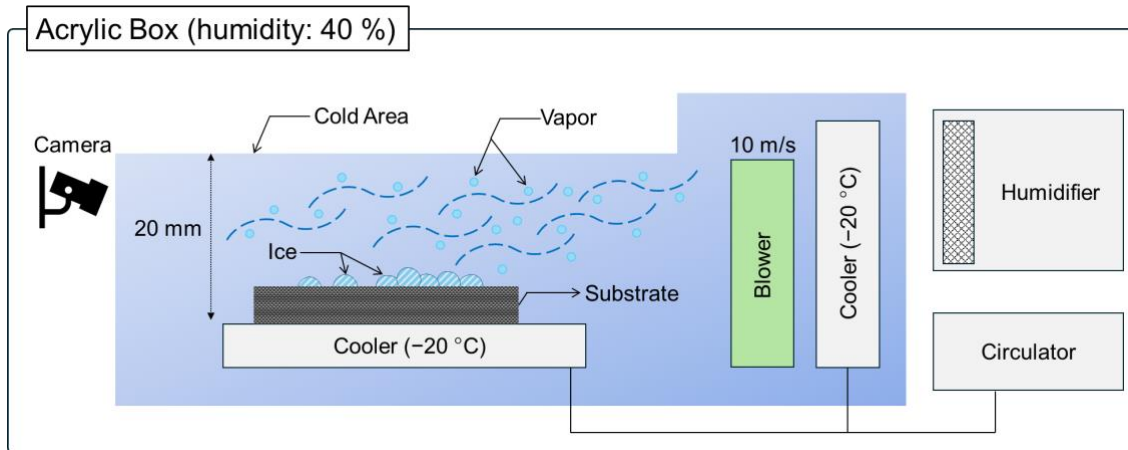
Figure 2. Schematic diagram of experimental setup for wind tunnel test.

3. Results and discussion

3.1. Characterization of surface morphology

Fig. 3a presents a 3D surface image of the specimen measured using a confocal microscope. It can be observed that the uncoated CFRP has scratches, and as the coating is applied, the surface of the CFRP becomes covered. In the case of a 0 % xylene content, it is noted that the shape of coating solution droplets remains even after curing. 10 % and 20 % of xylene concentration can be observed that the height where the droplets formed during spray coating is higher, but the shape of the coating solution does not remain. Xylene concentration is 30 %, almost no difference in the shape or height of the coating solution droplets was observed. Fig. 3b is a schematic diagram illustrating the behavior of droplets during coating. During spray coating, the coating solution ejected from the spray gun attaches to the CFRP and flows over the CFRP surface, covering it. The lower the viscosity of the coating solution, the higher its flowability on CFRP. Fig. S2 shows the viscosity of the PU topcoat coating solution at various xylene concentrations. Fig. 3c is a graph showing the results of the surface roughness measurement. The surface roughness of CFRP showed high values due to surface scratches. The decrease in surface roughness depends on the increasing concentration of xylene, which

results in the absence of remaining droplet shapes and a more uniform coating.
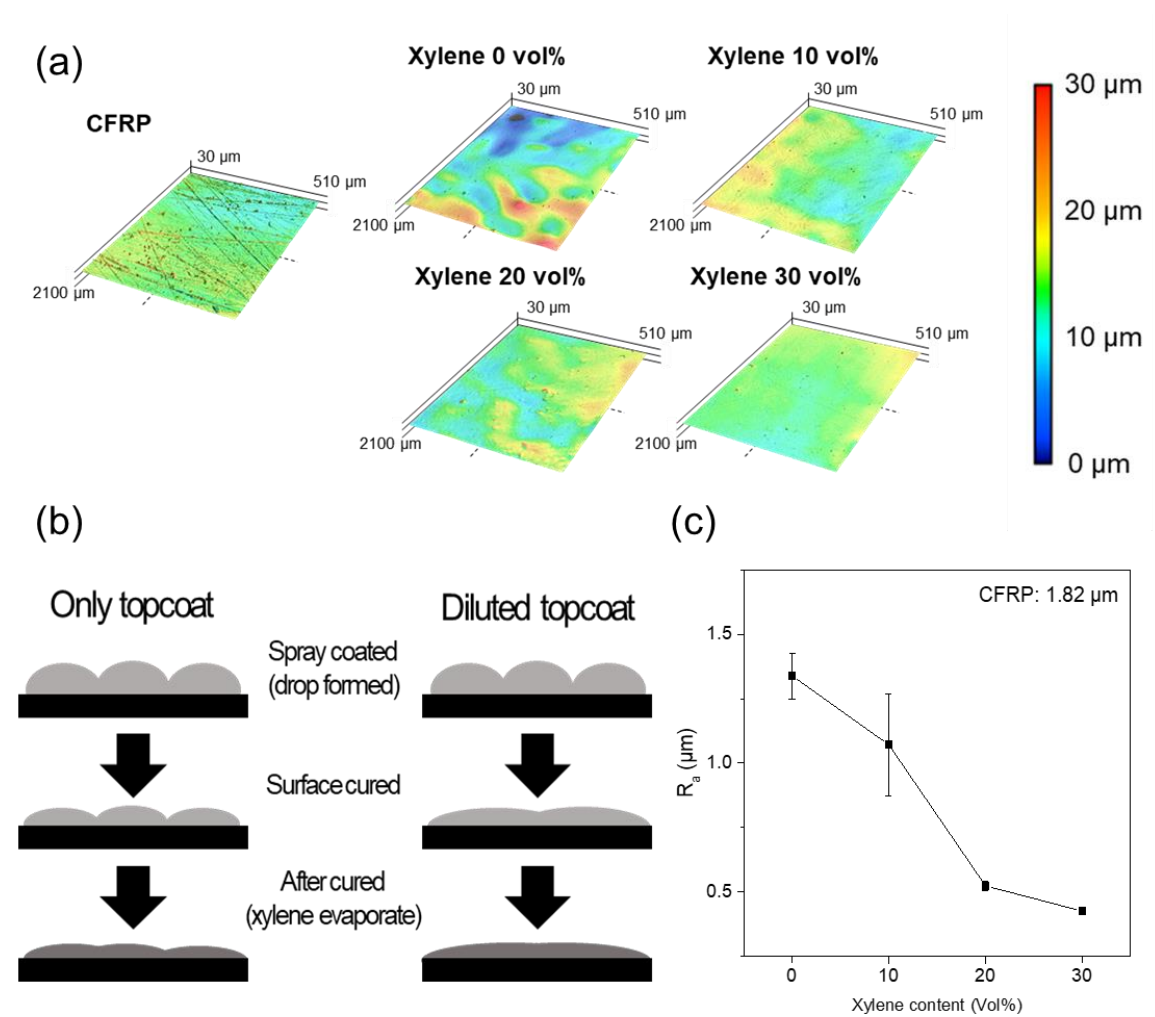

Figure 3. (a) 3D image of CFRP and PU topcoat, (b) behavior of PU topcoat droplets during coating, and surface roughness of PU topcoat depends on xylene content.

3.2. Characterization of the molecular structure and reactivity for PU

Fig. 4a presents the DSC curves during curing at different solvent concentrations. The curing reaction between alcohol and isocyanate to form PU is an exothermic reaction. Heating value released and the enthalpy change vary depending on the extent of the curing reaction between the two substances. As the solvent concentration increases, the concentration of the reactants

decreases, leading to a reduction in the reaction rate. As xylene, acting as a solvent, dilutes the mixture, the concentrations of alcohol and isocyanate decrease, thereby decreasing chances of intermolecular collisions. This leads to a decrease in reaction speed and a reduction in the amount of reaction products formed. Table 1 presents the curing times and heat of reaction (exothermic enthalpy changes) for PU depending on the concentration of the solvent used. When the enthalpy change was checked through the area of the exothermic peak in the graph, it was found that PU without added xylene had an enthalpy change of 249.9 J/g, while PU with 10 % added xylene had a significantly reduced enthalpy change of 49.1 J/g, indicating a reduction of approximately 200 J/g. The decrease in exothermic enthalpy during curing as the concentration of xylene increases. The difference in enthalpy changes correlates with the variation in the amount of urethane groups formed. For the curing times, a peak in heat release was observed at 104 min with 0 % xylene, at 128 min with 10 %, at 143 min with 20 %, and at 152 min with 30 %. According to reaction kinetics, a lower concentration of reactants results in a slower reaction rate, leading to a delayed appearance of the exothermic peak during curing.

Fig. 4b shows the FT-IR graph depends on xylene content. The C, O double bond of the urethane group can be identified in the range of 1680 cm^{-1} to 1750 cm^{-1}, and the C-O peak can be observed in the range of 1100 cm^{-1} to 1300 cm^{-1}. Here, the C-O peak is divided into peaks that appear from aliphatic ether groups and peaks from alcohol groups [39]. At around 1050 cm^{-1}, the C-O-C stretching vibration peak of aliphatic ether is observed, and at around 1200 cm^{-1}, the stretching vibration peak of alcohol is present. While the 0 % and 10 % samples show a greater number of C-O-C stretching vibration peaks of aliphatic ether, the 20 % and 30 % samples exhibit a higher number of stretching vibration peaks of alcohol [40]. As confirmed by DSC analysis, as the concentration of xylene increases, the quantity of reaction products decreases, and the reaction rate slows down. With the reduction in the quantity of

reaction products, the proportion of the urethane peak decreases, while the proportion of alcohol increases.

Fig. 4c presents the XRD data varying with the solvent concentration, where PU shows main peaks at $2\theta = 11$ °, 19 °, and 26 °. The appearance of peaks at $2\theta = 11$ ° indicates the presence of harder segments within PU, whereas peaks around $2\theta = 26$ ° suggest the presence of softer segments [41]. Fig. 4c presents the XRD data depend on xylene content, showing that PU displays main peaks at $2\theta = 11$ °, 19 °, and 26 °. The appearance of peaks at $2\theta = 11$ ° indicates the presence of harder segments in PU, whereas peaks around $2\theta = 26$ ° suggest softer segments. As the concentration of xylene decreases, the conversion rate of the reaction increases, leading to PU with harder segments. Grain size decreases as increasing xylene concentration to 25.9 nm, 21.5 nm, 20.4 nm, and 19.2 nm, indicating smaller PU crystals. A lower xylene concentration results in the agglomeration of PU chains, thereby increasing the size of the crystals. Furthermore, an increase in residual xylene can reduce the crystallinity. As the size of the crystals decreases, softer PU is formed.
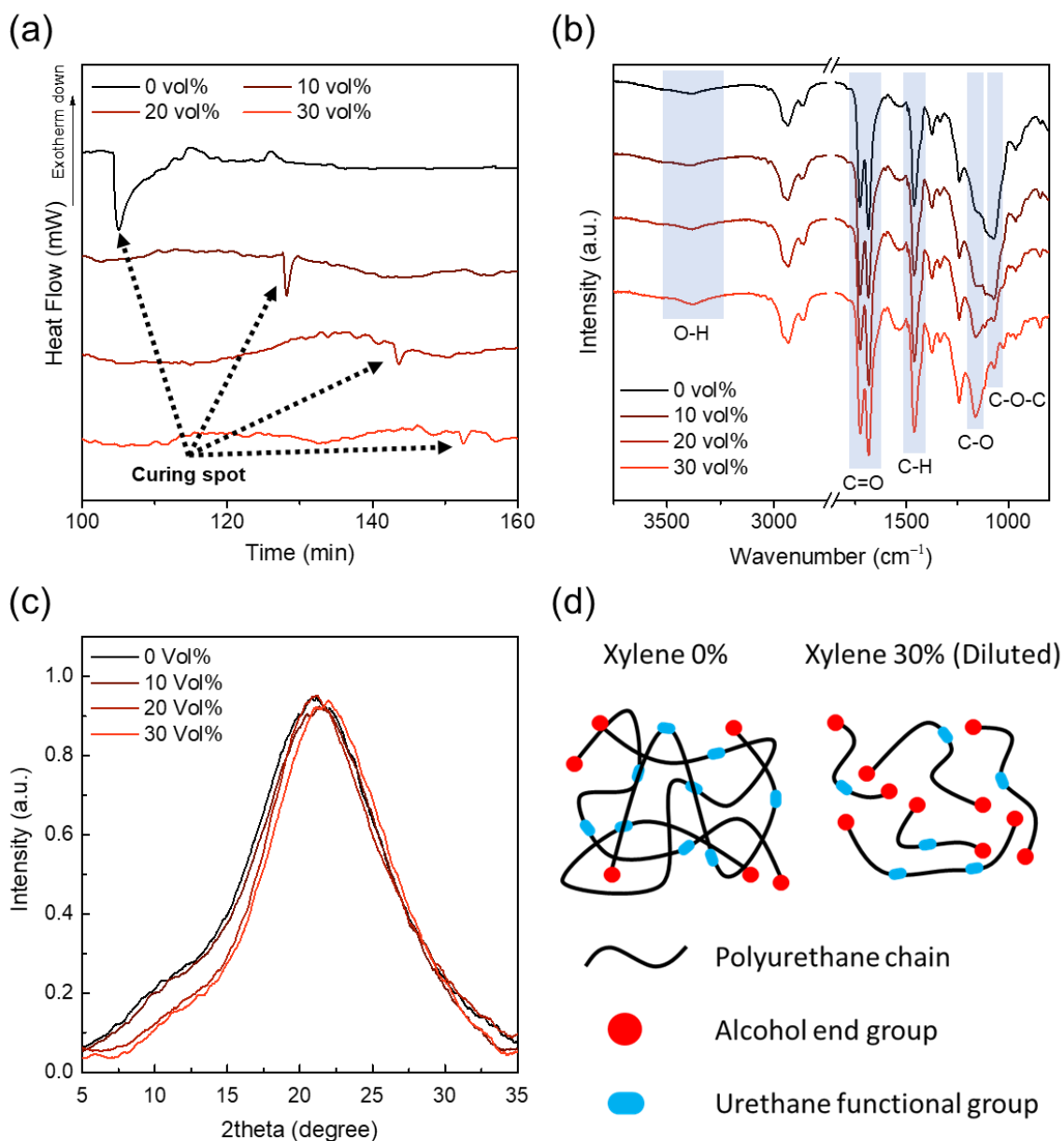
Figure 4. (a) DSC result of pretreated solution during curing depend on solvent amount (0, 10, 20, and 30 Vol% of xylene content), (b) FT-IR spectroscopy of PU-topcoat depends on solvent concentration after curing, (c) XRD data of PU-topcoat depend on solvent concentration, and (d) schematic diagram of the change in behavior of polymer chains depend on dilution in xylene.

Table 1. Curing time and enthalpy data of pretreated solution depend on xylene content by DSC measurement.

Sample name	0 Vol%	10 Vol%	20 Vol%	30 Vol%
Curing time (min)	104	128	143	152
$\triangle$H (J/g)	249.9	49.1	38.8	12.8

Table 2. 2θ and grain size of PU topcoat depend on xylene content through XRD measurement.

Sample name	0 Vol%	10 Vol%	20 Vol%	30 Vol%
2θ (°)	20.17	20.69	21.10	21.20
Grain size (nm)	25.9	21.5	20.4	19.2

3.3. Tensile properties of PU topcoat

Fig. 5a shows the stress-strain curve for the topcoat film during a tensile test according to the xylene content. The mechanical strength can vary depending on the crosslinking density of PU. As the concentration of xylene increases, the amount of reaction product decreases, and the crosslinking density becomes lower. A decrease in crosslinking density results in lower mechanical strength. Our MD simulations also supported the decrease of mechanical strength by confirmation of increase of FFV of PU system as increase of xylene concentration (Figure S5). Fig. 5b is tensile strength, tensile strain, and Young's modulus depends on xylene content. The tensile strength decreases as the content of xylene increases. Tensile strain and Young's modulus show a consistent pattern up to a xylene concentration of 0, 10, and 20 %, but decrease at 30 %. This is due to the formation of soft segments at 30 %, as confirmed by XRD. Observing the results for Young's modulus, it can be seen that the standard deviation decreases as the concentration of xylene increases, indicating that the structure and crystals of PU are uniformly formed at 30 %.
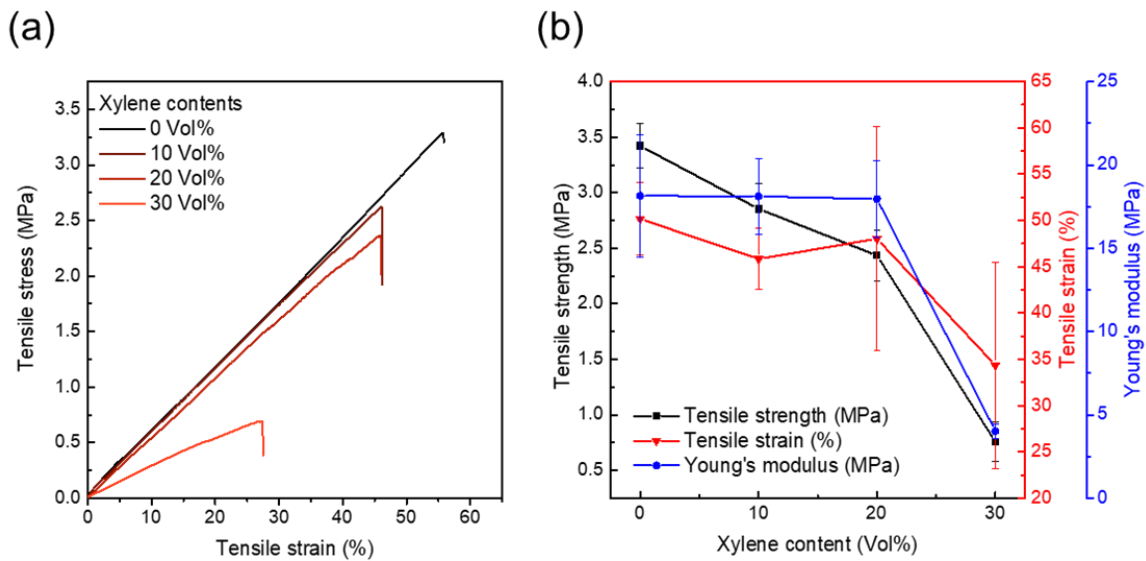
Figure 5. (a) Stress-strain curve of PU topcoat depend on xylene content from 0 to 30 Vol% and (b) tensile strength, tensile strain, and Young's modulus depend on xylene content.

3.4. Changes in contact angle and surface analysis depends on molecular structure of PU

Generally, contact angle and surface energy vary depending on the surface hydrogen bonding and molecular configuration. Fig. 6a represents the graph of results for contact angle and surface energy depends on the solvent concentration. Contact angle on PU topcoat was found to be higher than CFRP. Molecular structure of PU, centered around hydrocarbon groups, forms a symmetrical structure with low polarity, whereas the molecular structure of epoxy possesses alcohol groups after curing, resulting in higher polarity. Therefore, in this study, by coating PU on CFRP, the polar surface energy decreased, and as a result, the contact angle increased. In the case of PU, it possesses polyol and isocyanate groups before curing, exhibiting polarity, but after curing, it binds into urethane groups, resulting in decreased polarity. With xylene content of 0, 10, 20, and 30 %, γ values were observed to be 31.2 dyne/cm, 29.5 dyne/cm, 28.6

dyne/cm, and 29.5 dyne/cm, respectively, and γ^P values were found to be 12.21 dyne/cm, 9.39 dyne/cm, 9.36 dyne/cm, and 9.47 dyne/cm, respectively. In the sample with 0 % solvent concentration, the curing reaction speed is fast, leading to non-uniform reaction progress, which can result in unreacted alcohol groups increasing the surface energy.

Fig. 6b is a graph where work of adhesion for water and ice on the substrate is calculated using formula 6, by adjusting the solvent concentration. The work of adhesion at the interface varies due to interactions caused by the secondary bonding between the two materials. Work of adhesion, depends on xylene content, shows a trend similar to that of surface energy, with the lowest work of adhesion observed at a xylene concentration of 20 %. This indicates that at a xylene concentration of 20 %, the interactions with water or ice are minimized.

Fig. 6c is a schematic diagram about the effect of solvent concentration adjustment on the water contact angle of the formed PU topcoat. As the concentration of xylene decreases, the reaction rate increases. With the increase in reaction rate, the formation of PU is relatively uneven, leading to areas that are not uniformly developed. These unevenly formed areas cause an increase in surface energy [42]. When the xylene content is 0%, the reaction occurs most rapidly, leading to uneven formation and thus higher interaction with water. As the xylene content increases, the reaction rate slows down, resulting in a more uniform formation. Consequently, as the xylene content increases, the contact angle also increases. Changes in segments were observed at a xylene concentration of 30 %, as confirmed by XRD [43]. These changes in properties appear to have led to a relatively lower contact angle.
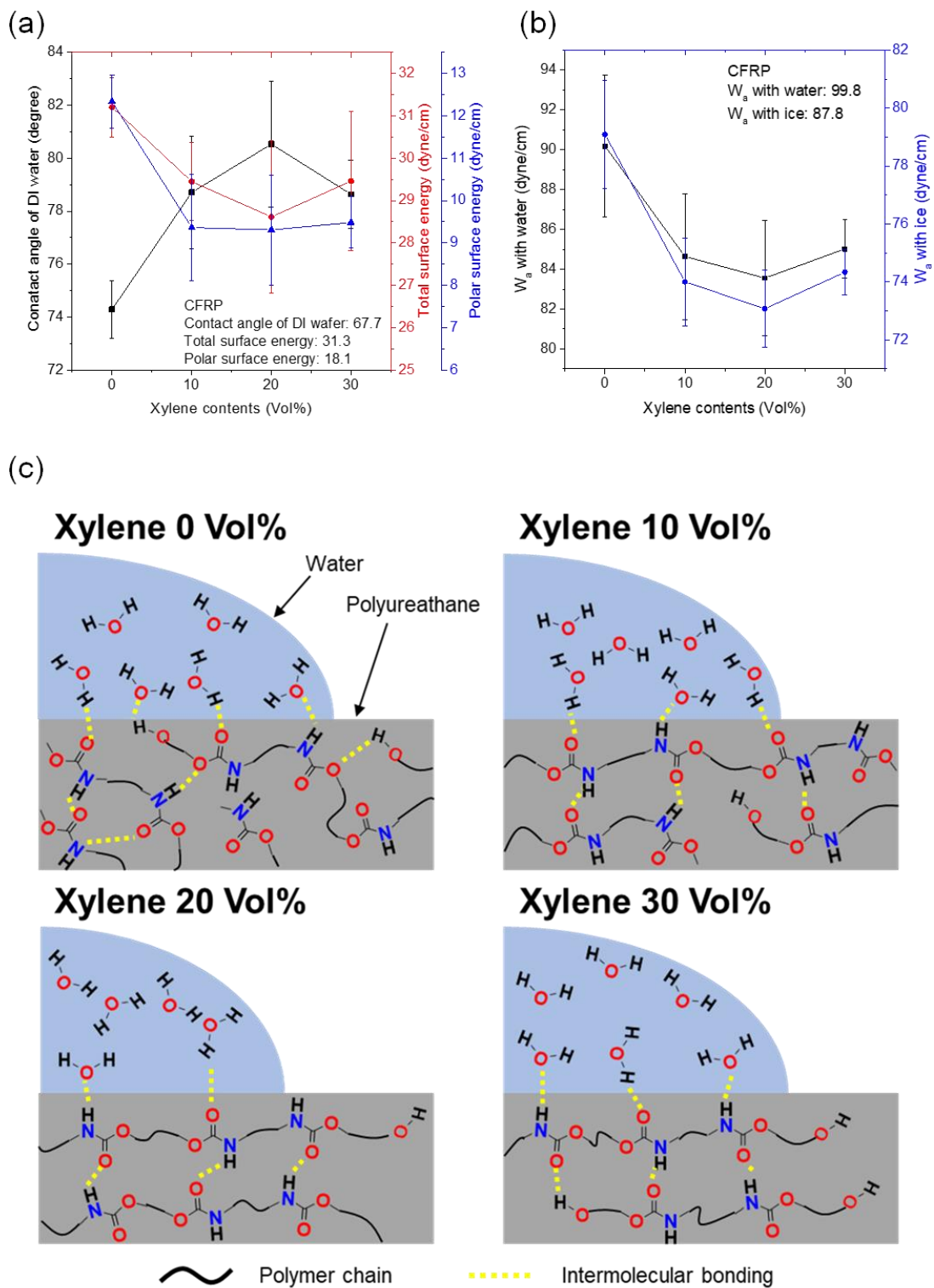
Figure 6. (a) Static contact angle and surface energy of PU topcoat depends on xylene content, (b) work of adhesion on PU topcoat with water and ice depend on to xylene content, and (c) schematic diagram of molecular behavior and secondary bonding in various PU topcoat.

3.5. Characterization of deicing properties depends on molecular structure of PU

Fig. 7a presents the experimental results regarding icing. The application of a PU coating, which is more hydrophobic than epoxy, delayed the initial icing. The specimen with 20 % concentration, which had the lowest surface energy, exhibited the highest ice delay effect. As the surface hydrophobicity increases, the likelihood of ice adhesion to the surface decreases, thereby delaying icing [44]. As a result, the amount of ice grown or accumulated over the same period of time is reduced [45, 46]. Fig. 7b shows photographs at the time of icing and after 600 s. After the same duration of 600 s, it was observed that the 20 % concentration specimen had the least amount of icing. While the 20 % concentration showed the best performance in delaying surface icing in repeated experiments, the 30 % concentration, which has a lower surface roughness, demonstrated the best retention. The structural change of the polymer to a softer state at a xylene concentration of 30 % is found to enhance long-term durability.
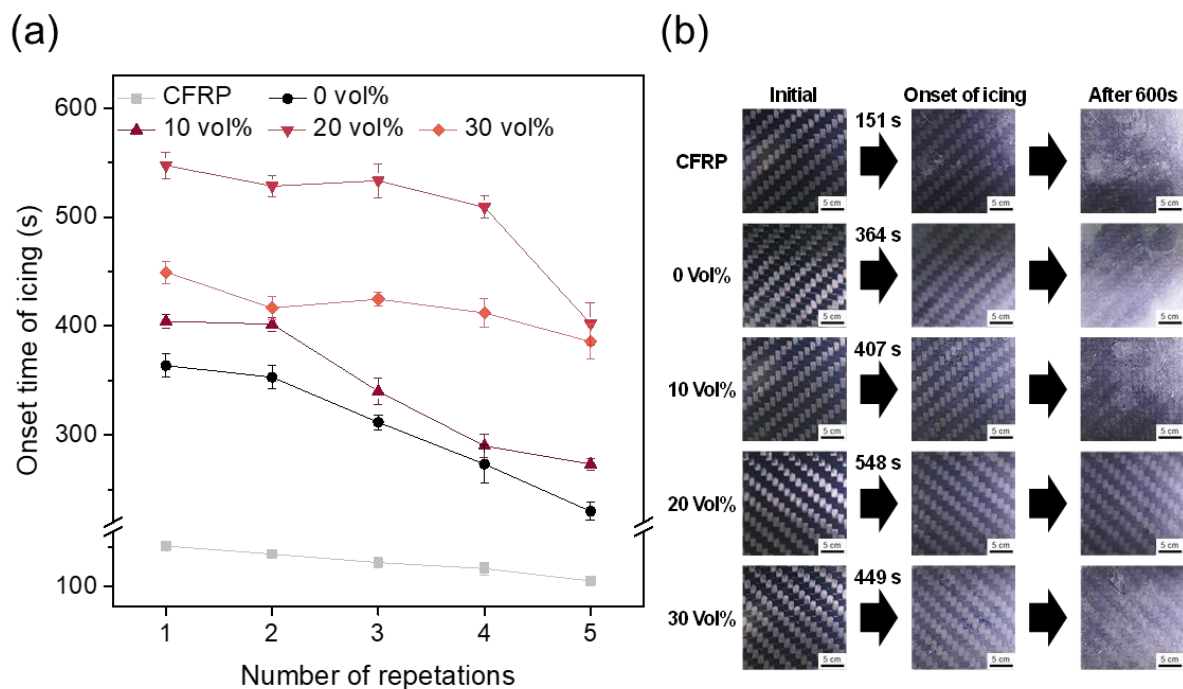
Figure 7. (a) Graph of freezing test and repetition of CFRP and PU topcoat depend on xylene content, (b) photographic images of initial state, icing and freeze growth after 600s of CFRP and PU topcoat depend on xylene content.

Fig. 8a presents schematic diagram of movement of water vapor and ice during a wind tunnel test. As in the schematic diagram, it can be observed that ice formation begins on the side facing the incoming wind. This occurs because ice forms when supercooled water vapor comes into contact with a cold surface and solidifies, resulting in ice formation in the direction from which the wind is carrying the water vapor. Fig. 8b displays a progression of images detailing changes to the surface over time in a wind tunnel test. Due to the wind blowing from the right, ice formation commenced on the right side of the specimen. Ice formation exhibited similar characteristics to those observed during tests conducted in a static environment. CFRP had such extensive ice formation on its surface that the arrangement of carbon fibers was no longer visible. Similarly, after 10 min, the fiber arrangement could not be seen at 0 %. As the xylene content increased to 10 % and 20 %, the amount of ice formation decreased. However, when the xylene content reached 30 %, ice formation increased.

Figure 8. (a) Schematic diagram of movement of water vapor and ice during a wind tunnel test and (b) images of ice formation on CFRP and PU Topcoat over time under dynamic conditions.

4. Conclusion

In this study, the effect of polymer structure on delaying surface icing was investigated. By diluting polyurethane topcoat in xylene, changes were induced in the polymer's structure and crystallinity. The degree of polyurethane curing reactions, molecular structure, and crystallinity in response to varying concentrations of xylene were assessed using DSC, FT-IR, and XRD techniques. It was observed that an increase in xylene concentration led to an increase in the free volume within the molecular structure, and a consequent decline in the mechanical properties of the topcoat. Changes of polymer structure resulted in changes to the surface energy. Surface energy at a 20 % xylene concentration was the lowest, recorded at 28.6 dyne/cm, which also corresponded to reduced work of adhesion with ice. Icing was about 1.7 times more likely at a 20 % concentration, which had the lowest affinity towards water and ice compared to 0 %, yet the deicing performance demonstrated the highest durability at a 30 % concentration. This revealed that the polymer structure, modified by the diluent used for enhancing processability among other factors, significantly influences the delay in icing.

Acknowledgement

CRediT authorship contribution statement

Declaration of Competing Interest

The authors declare that they have no known competing financial interests or personal relationships that could have appeared to influence the work reported in this paper.

References

[1] Y. Cao, W. Tan, Z. Wu, Aircraft icing: An ongoing threat to aviation safety, Aerospace Science and Technology, 75 (2018) 353-385.

[2] D. Zeng, Y. Li, H. Liu, Y. Yang, L. Peng, C. Zhu, N. Zhao, Superhydrophobic coating induced anti-icing and deicing characteristics of an airfoil, Colloids and Surfaces A: Physicochemical and Engineering Aspects, 660 (2023).

[3] O. Parent, A. Ilinca, Anti-icing and de-icing techniques for wind turbines: Critical review, Cold Regions Science and Technology, 65 (2011) 88-96.

[4] Z. Zhao, H. Chen, X. Liu, H. Liu, D. Zhang, Development of high-efficient synthetic electric heating coating for anti-icing/de-icing, Surface and Coatings Technology, 349 (2018) 340-346.

[5] X. Liu, H. Liu, Y. Li, F. Teng, C. Liang, Superhydrophobic surface of hybrid nanocomposites made of TiO2 and multi-walled carbon nanotubes: Photothermal ice removal performance and wear resistance, Applied Surface Science, 640 (2023).

[6] S. Rabbani, E. Bakhshandeh, R. Jafari, G. Momen, Superhydrophobic and icephobic polyurethane coatings: Fundamentals, progress, challenges and opportunities, Progress in Organic Coatings, 165 (2022).

[7] L. Wang, K. Yin, Q. Deng, Q. Huang, C.J. Arnusch, Multiscale hybrid-structured femtosecond laser-induced graphene with outstanding photo-electro-thermal effects for all-day anti-icing/deicing, Carbon, 219 (2024).

[8] Z. Xie, H. Wang, Y. Geng, M. Li, Q. Deng, Y. Tian, R. Chen, X. Zhu, Q. Liao, Carbon-Based Photothermal Superhydrophobic Materials with Hierarchical Structure Enhances the Anti-Icing and Photothermal Deicing Properties, ACS Appl Mater Interfaces, 13 (2021) 48308-48321.

[9] B. Wang, P. Yu, Q. Yang, Z. Jing, W. Wang, P. Li, X. Tong, F. Lin, D. Wang, G.E. Lio, R. Caputo, O. Ávalos-Ovando, A.O. Govorov, H. Xu, Z.M. Wang, Upcycling of biomass waste into photothermal superhydrophobic coating for efficient anti-icing and deicing, Materials Today Physics, 24 (2022).

[10] T. Xiang, X. Chen, Z. Lv, W. Tong, J. Cao, Y. Shen, B. Liao, Y. Xie, S. Zhang, Stable photothermal solid slippery surface with enhanced anti-icing and de-icing properties, Applied Surface Science, 624 (2023).

[11] R. Dou, J. Chen, Y. Zhang, X. Wang, D. Cui, Y. Song, L. Jiang, J. Wang, Anti-icing coating with an aqueous lubricating layer, ACS Appl Mater Interfaces, 6 (2014) 6998-7003.

[12] J. Zhou, H. Xu, L. Tang, Facile fabrication of high performance hydrophilic anti-icing polyurethane methacrylate coatings cured via UV irradiation, Progress in Organic Coatings, 182 (2023).

[13] P. Irajizad, S. Nazifi, H. Ghasemi, Icephobic surfaces: Definition and figures of merit, Adv Colloid Interface Sci, 269 (2019) 203-218.

[14] M. Jung, T. Kim, H. Kim, R. Shin, J. Lee, J. Lee, J. Lee, S. Kang, Design and fabrication of a large-area superhydrophobic metal surface with anti-icing properties engineered using a top-down approach, Applied Surface Science, 351 (2015) 920-926.

[15] Y. Xue, Y. Wang, X. Sui, W. Liang, F. Wang, Superhydrophobic, photothermal, MXene/PEI composite film with anti-icing and deicing properties, Materials Letters, 347 (2023).

[16] F. Wang, T.E. Tay, Y. Sun, W. Liang, B. Yang, Low-voltage and -surface energy SWCNT/poly(dimethylsiloxane) (PDMS) nanocomposite film: Surface wettability for passive anti-icing and surface-skin heating for active deicing, Composites Science and Technology, 184 (2019).

[17] S.A. Kulinich, M. Farzaneh, On ice-releasing properties of rough hydrophobic coatings, Cold Regions Science and Technology, 65 (2011) 60-64.

[18] Q. Liu, Y. Yang, M. Huang, Y. Zhou, Y. Liu, X. Liang, Durability of a lubricant-infused Electrospray Silicon Rubber surface as an anti-icing coating, Applied Surface Science, 346 (2015) 68-76.

[19] C.-H. Xue, H.-G. Li, X.-J. Guo, Y.-R. Ding, B.-Y. Liu, Q.-F. An, Y. Zhou, Superhydrophobic anti-icing coatings with self-deicing property using melanin nanoparticles from cuttlefish juice, Chemical Engineering Journal, 424 (2021).

[20] T. Bharathidasan, S.V. Kumar, M.S. Bobji, R.P.S. Chakradhar, B.J. Basu, Effect of wettability and surface roughness on ice-adhesion strength of hydrophilic, hydrophobic and superhydrophobic surfaces, Applied Surface Science, 314 (2014) 241-250.

[21] S. Yang, Q. Xia, L. Zhu, J. Xue, Q. Wang, Q.-m. Chen, Research on the icephobic properties of fluoropolymer-based materials, Applied Surface Science, 257 (2011) 4956-4962.

[22] A. Khadak, B. Subeshan, R. Asmatulu, Studies on de-icing and anti-icing of carbon fiber-reinforced composites for aircraft surfaces using commercial multifunctional permanent superhydrophobic coatings, Journal of Materials Science, 56 (2020) 3078-3094.

[23] Y.-H. Ng, S.W. Tay, L. Hong, Ice-phobic polyurethane composite coating characterized by surface micro silicone loops with crumpling edges, Progress in Organic Coatings, 172 (2022).

[24] Y. Wu, L. Dong, Q. Ran, Facile one-step spraying preparation of fluorine-free transparent superhydrophobic composite coatings with tunable adhesion for self-cleaning and anti-icing applications, Applied Surface Science, 649 (2024).

[25] X. Wu, Y. Pan, Z. Han, Y. Shen, Does Anti-Condensation coatings guarantee Anti-Icing Properties?, Applied Surface Science, 649 (2024).

[26] S. Brown, J. Lengaigne, N. Sharifi, M. Pugh, C. Moreau, A. Dolatabadi, L. Martinu, J.E. Klemberg-Sapieha, Durability of superhydrophobic duplex coating systems for aerospace applications, Surface and Coatings Technology, 401 (2020).

[27] J. Bang, H. Choi, K.-S. Ahn, H. Yeo, J.-K. Oh, H. Won Kwak, Sustainable cellulose nanofiber/hydrophobic silica nanoparticle coatings with robust hydrophobic and water-resistant properties for wood substrates, Applied Surface Science, 654 (2024).

[28] M. Osterhold, Scratch/mar, surface structure and rheology measurements, Progress in Organic Coatings, 161 (2021).

[29] T. Mariappan, A. Kamble, S.M. Naik, An investigation of primer adhesion and topcoat compatibility on the waterborne intumescent coating to structural steel, Progress in Organic Coatings, 131 (2019) 371-377.

[30] M. Sahadat Hossain, S. Tarannum, M. Kawsar, N.M. Bahadur, S. Ahmed, Synthesis of pure and Cd-doped hydroxyapatite for the photo-catalytic degradation of Amoxicillin and Ciprofloxacin: Crystallographic characterization using XRD, Journal of Hazardous Materials Advances, 13 (2024).

[31] R.L.C. Akkermans, N.A. Spenley, S.H. Robertson, COMPASS III: automated fitting workflows and extension to ionic liquids, Molecular Simulation, 47 (2020) 540-551.

[32] H.J.C. Berendsen, J.P.M. Postma, W.F. van Gunsteren, A. DiNola, J.R. Haak, Molecular dynamics with coupling to an external bath, The Journal of Chemical Physics, 81 (1984) 3684-3690.

[33] N. Dilsiz, J.P. Wightman, Effect of acid–base properties of unsized and sized carbon fibers on fiber/epoxy matrix adhesion, Colloids and Surfaces A: Physicochemical and Engineering Aspects, 164 (2000) 11.

[34] D. Zhang, An Equation-of-State approach to measure the surface free energy (SFE) of bituminous binders, Measurement, 158 (2020).

[35] F.M. Fowkes, ADDITIVITY OF INTERMOLECULAR FORCES AT INTERFACES. I.

DETERMINATION OF THE CONTRIBUTION TO SURFACE AND INTERFACIAL TENSIONS OF DISPERSION FORCES IN VARIOUS LIQUIDS, The Journal of Physical Chemistry, 67 (1963) 4.

[36] D.J. Król, A. Wymysłowski, K.N. Allaf, Adhesion work analysis through molecular modeling and wetting angle measurement, Microelectronics Reliability, 55 (2015) 758-764.

[37] W. Guo, H. Shen, Y. Li, F. Feng, K. Tagawa, Wind tunnel tests of the rime icing characteristics of a straight-bladed vertical axis wind turbine, Renewable Energy, 179 (2021) 116-132.

[38] Q. Wang, X. Yi, Y. Liu, J. Ren, J. Yang, N. Chen, Numerical investigation of dynamic icing of wind turbine blades under wind shear conditions, Renewable Energy, 227 (2024).

[39] A. Colin, M. Baba, P.O. Bussiere, E. Cavaletti, F. Nizeyimana, S. Therias, Investigation of the thermo-oxidation mechanism of acrylic-urethane-silicone/amino-silane based topcoat, Polymer Degradation and Stability, 114 (2015) 115-124.

[40] J.W. Diehl, J.W. Finkbeiner, F.P. DiSanzo, Determination of Ethers and Alcohols in Gasolines by Gas Chromatography/Fourler Transform Infrared Spectroscopy, ANALYTICAL CHEMISTRY, 64 (1992) 3202.

[41] G. Trovati, E.A. Sanches, S.C. Neto, Y.P. Mascarenhas, G.O. Chierice, Characterization of polyurethane resins by FTIR, TGA, and XRD, Journal of Applied Polymer Science, 115 (2009) 263-268.

[42] M. Shi, T. Wang, Y. Wu, R. Sun, W. Wang, J. Guo, Q. Wu, W. Yang, J. Min, The Intrinsic Role of Molecular Mass and Polydispersity Index in High-Performance Non-Fullerene Polymer Solar Cells, Advanced Energy Materials, 11 (2020).

[43] C. Zhang, J. Hu, S. Chen, F. Ji, Theoretical study of hydrogen bonding interactions on MDI-based polyurethane, J Mol Model, 16 (2010) 1391-1399.

[44] L.B. Boinovich, A.M. Emelyanenko, Anti-icing Potential of Superhydrophobic Coatings, Mendeleev Communications, 23 (2013) 3-10.

[45] T.M. Schutzius, S. Jung, T. Maitra, P. Eberle, C. Antonini, C. Stamatopoulos, D. Poulikakos, Physics of icing and rational design of surfaces with extraordinary icephobicity, Langmuir, 31 (2015) 4807-4821.

[46] S. Cheng, P. Guo, X. Wang, P. Che, X. Han, R. Jin, L. Heng, L. Jiang, Photothermal slippery surface showing rapid self-repairing and exceptional anti-icing/deicing property, Chemical Engineering Journal, 431 (2022).